# $^{26}$Al–$^{26}$Mg isotopic studies in some calcium–aluminium-rich inclusions and chondrules from unequilibrated chondrites

**Ritesh Kumar Mishra[1,2,3,*], Kuljeet Kaur Marhas[4] and Mario Trieloff[1]**

[1]Klaus-Tschira-Labor für Kosmochemie, Institut für Geowissenschaften, Im Neuenheimer Feld 234-236 Ruprecht-Karls-Universität, Heidelberg, D-69210, Germany
[2]National Museum of Natural History, Smithsonian Institution, Washington, DC, USA
[3]Present address: Independent Researcher, Dhawalpur Village, PO Kaitha, Bhagalpur 813 211, India
[4]Planetary Sciences Division, Physical Research Laboratory, Navrangpura, Ahmedabad 380 009, India

**Calcium–aluminium-rich inclusions (CAIs) and chondrules are the oldest dated components of chondrites. They record the events and processes during the formation and early evolution of the solar system in their morphology, mineral phases and isotopic compositions. $^{26}$Al–$^{26}$Mg isotopic systematics of two CAIs from Leoville (CV3.1-3.4), two chondrules from Queen Alexandra range 99177 (CR3.00), one mega chondrule from Semarkona (LL3.00), and a plagioclase rich chondrule from Chainpur (LL3.4) were carried out to understand the formation processes of these rare kinds of objects and to obtain constraints on early solar system events and processes. Petrographic and isotopic properties of Leoville CAI 1 (Type B2) suggest its formation c. 0.1 Ma after typical non-igneous CAIs characterized by the canonical ratio of $^{26}$Al/$^{27}$Al = 5.25 × 10$^{-5}$, from a partial melt heated to a maximum temperature of ~1420°C and cooled slowly at ≤0.5°C/h. Leoville CAI 3 (Type A) plausibly formed early within 1 Ma of the canonical CAI value and subsequently experienced parent body aqueous alteration. The analysed chondrules did not yield significant $^{26}$Mg excess due to their small Al/Mg ratio or resetting by secondary processes.**

**Keywords:** Calcium–aluminium-rich inclusions, chondrules, early solar system relative chronology, short-lived now-extinct radionuclide, solar system.

THE decay of short-lived now-extinct radionuclide (SLN) $^{26}$Al into $^{26}$Mg (half-life $T_{½}$ = 0.72 Ma) has long been used as a useful relative chronometer to study the origin and early evolution (few ten million years) of the solar system[1–3]. Chondrites, in particular, are a repository of the earliest solar system solids consisting of calcium–aluminium-rich inclusions (CAIs), chondrules, metal-sulphide grains and fine-grained matrix that accreted to form larger-sized bodies of the solar system[4]. Only a miniscule few of them, under fortuitous conditions, escaped nebular and parent body thermal and aqueous alteration and are designated as unequilibrated chondrites belonging to the lowest petrographic grade 3.0 in the petrographic scale[5–7] ranging from 1 to 6. The minimally altered unequilibrated chondrites are of special importance and potential for obtaining the primitive records of the solar system. In the present study, we have selected a few CAIs and chondrules from the unequilibrated chondrites (petrographic grade 3.0–3.4) for $^{26}$Al–$^{26}$Mg isotopic studies. The selected objects have properties (e.g. size, composition) that are rare and suitable for carrying out multiple radiogenic and stable isotope studies. Petrographic and mineralogical characterization of some of these objects were carried out to constrain their petrogenesis.

## Analytical method, meteorites and analysed objects

### *Analytical procedure*

*Imaging, elemental abundances and phase characterization:* The electron beam imaging, X-ray elemental abundances were obtained using field-emission scanning electron microscope FE-EPMA JEOL 8530F hyper probe at NASA Johnson Space Center in Houston, USA, and scanning electron microscope LEO 440 at the Institut für Geowissenschaften, Ruprecht-Karls-Universität, Heidelberg, Germany. Phase characterization was carried out using electron probe microanalyser FE-EPMA JEOL 8530F hyper probe at the NASA Johnson Space Center in Houston, USA. A 10–20 nA, 15–20 keV electron beam of ~1 μm size was used to obtain back-scattered electron (BSE) images and rastered over the sample to obtain elemental abundances using Oxford Silicon Drift Detector type energy dispersive spectrometer (EDS). For quantification of mineral phases, a 20 keV accelerated electron beam of 15–20 nA was focussed to a spot of size 1–2 μm to obtain characteristic X-rays which were measured in wavelength dispersive mode using the available large lithium flouride, lithium flouride, TAP, polyethelene terephthalate, large polyethelene terephthalate crystals. Typically, Na, K were measured first for 15 sec,

*For correspondence. (e-mail: riteshkumarmishra@gmail.com)

while the background counts of the detectors were measured for 10 sec. The other elements were measured for 30 sec, while the background was measured for 20–30 sec. ZAF (Z – atomic number, stopping power; A – absorption; F – fluorescence) procedure was used for matrix correction. Well-characterized industry metal and mineral standards and terrestrial samples (e.g. Sitkhin anorthite, Burma spinel, Madagascar hibonite, San Carlos olivine) analogous to the mineral phases in the meteorites were measured prior to and sometimes after the analysis of the meteorite samples.

*$^{26}$Al–$^{26}$Mg isotopic analysis:* $^{26}$Al–$^{26}$Mg isotope systematics were performed using the secondary ion mass spectrometer Cameca 1280 HR2 at Institut für Geowissenschaften, Heidelberg, Germany. A focussed primary ~15 μm size $O^-$ beam of ~0.15 nA was used to sputter the samples for positive secondary ions of $^{24}$Mg, $^{25}$Mg, $^{26}$Mg and $^{27}$Al. The primary beam accelerated by 13 kV, and the sample kept at –10 kV combined gave an impact energy of 23 keV for the primary beam to sputter the upper few atomic layers of the polished and coated samples of the meteorites and standards. The secondary ions accelerated by 10 kV energy were sorted by the electrostatic sector, and focussed, and shaped using multiple electrostatic lenses and deflectors before passing through the magnetic sector to obtain double focussing in mass and energy of separated ions at the detector plane by cyclic switching of the calibrated magnetic field values for the desired isotopes. High mass resolution (HMR = M/ΔM, 5–95%) of >4500 was used to resolve all the major hydride interferences of $NaH^+$ in $^{24}$Mg, $MgH^+$ in $^{25}$Mg, $^{26}$Mg and $^{27}$Al as well as isobaric interference in $^{24}$Mg due to doubly charged $^{48}Ca^{++}$ and $^{48}Ti^{++}$. An energy filter window of 60 eV was used to limit the chromatic, non-axial errors associated with the electric-magnetic optical system[8]. Magnesium isotopes were measured using an axial electron multiplier by switching (peak jumping) to suitable magnetic field values, while $^{27}$Al was measured concurrently with $^{25}$Mg on Faraday cup H′2. In the mono-multi combined mode $^{24}$Mg, $^{25}$Mg and $^{26}$Mg were measured typically for 3, 5 and 5 sec respectively, with waiting times of 3, 2 and 2 sec. The mono-multicollection combined mode was adopted to measure a large range of Mg abundance within the different minerals in CAIs and chondrules. For the synthetic melilite composition glass (Åk ~70%, MgO = 9.4 wt.%), $^{24}$Mg and $^{27}$Al cps of ~$4.5 \times 10^5$ and $8.2 \times 10^5$ were measured with the analytical protocol. Dead time corrections (55 ns) were applied to measured count rates by the electron multiplier. During a typical session, the measurement analytical uncertainty in $\delta^{25}$Mg for melilite glass was ~0.5 per mil (‰) ($2\sigma$, SD) with external reproducibility of ~0.74‰ ($2\sigma$, SD). The sum of counts was used to calculate isotopic ratios. The analytical protocol adopted for the present study was in anticipation of a large range of expected count rates for a diverse set of minerals found in CAIs and chondrules. Hence, the study does not utilize the full analytical capacity of the instrument, but the protocol allows it to accommodate the diversity of minerals with the simple approach without losing the prime expected information for the analysed objects. This approach is reasoned with the larger objective of accomplishing multiple *in situ* radiogenic and stable isotopic studies in these 'rare' objects; the first of which is presented here. Several terrestrial standards (Burma spinel, MORB glasses) and synthetic glasses (åkermanite (Åk) ~20, Åk ~70, Ca-Px, anorthite (MgO ~1.8 wt%)), analogous to mineral phases in CAIs and chondrules encompassing a range of abundance of Al, Mg and Al/Mg ratios were used for calibration and obtaining relative sensitivity factors[9]. With the adopted analytical protocol, these samples show a range of mass fractionation from –12 to –3‰ (±2; $2\sigma$). The instrumental mass fractionation observed in synthetic standards analogous to the mineral phases in meteorite samples (e.g., synthetic Åk glass for melilite, synthetic anorthite glass for anorthite) was used for instrumental mass fractionation correction.

Mass fractionation corrected excess in $^{26}$Mg in meteorites was calculated using the equation:

$$\delta^{i}\mathrm{Mg} = [(^{i}\mathrm{Mg}/^{24}\mathrm{Mg})_{\mathrm{measured}}/(^{i}\mathrm{Mg}/^{24}\mathrm{Mg})_{\mathrm{standard}} - 1]*1000; \quad i = 25, 26,$$

$$\Delta^{26}\mathrm{Mg} = \delta^{26}\mathrm{Mg} - [(1 + \delta^{25}\mathrm{Mg}/1000)^{\beta} - 1] * 1000,$$

where $^{25}$Mg/$^{24}$Mg = 0.12663, $^{26}$Mg/$^{24}$Mg = 0.13932 (ref. 10), $\beta = 0.5128$ (ref. 11). Standard deviations of measurements in the meteorite samples were added in quadrature to standard errors of the standards to obtain the reported errors.

## *Meteorites and analysed objects*

*Leoville $CV_{red}$ 3.1-3.4:* Leoville meteorite, a ~8.1 kg 'find' (1961, Decatur, Kansas, USA), is a reduced carbonaceous chondrites of Vigarano type that is classified as 3.1–3.4 with evidences of preservation of both pristine characteristics and alterations within[5,6]. A thin section of Leoville of ~1.2 cm × 0.8 cm has three CAIs, 2 amoeboid olivine aggregates and ~9 chondrules of different sizes and types. Two CAIs from Leoville were selected for the present study.

## *Petrography and mineralogy of Leoville CAIs*

Leoville CAI 1 is a large ovoid-shaped Type B2 CAI of ~7.5 × 7.5 mm size (Figure 1 *a–d*). The CAI is composed largely of melilite with subordinate spinel, pyroxene and anorthite (Table 1, Figure 1 *c*). Melilites are typically blocky with grain sizes of 300–700 μm. They are zoned, showing a gradient in the abundance of aluminium decreasing towards the edges of the grains (Figure 1 *b*). A profile of melilite composition from core to periphery of the CAI indicated by a dotted arrow (line 1 in Figure 1 *a*) is shown in Figure 2 *a*. The variation in melilite composition in a melilite grain and the outermost region up to the rim is also

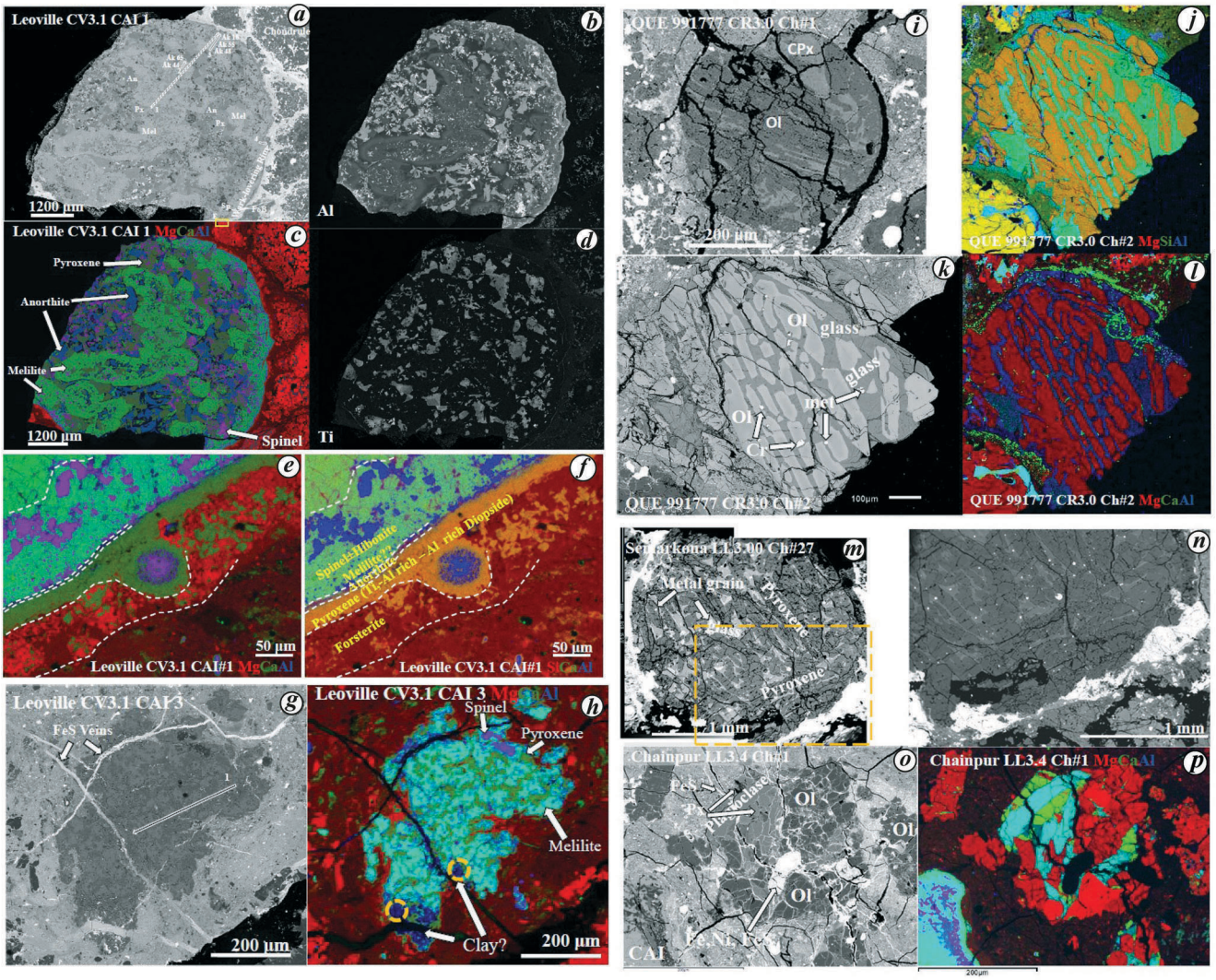


**Figure 1.** Back-scattered electron (BSE) images and false coloured mosaic images of the studied CAIs and chondrules from unequilibrated chondrites. ***a***, ***g***, ***i***, ***k***, ***m***, ***o*** show BSE image of Leoville CAI 1, Leoville CAI 3, QUE 99177 Ch 1, QUE 99177 Ch 2, Semarkona Ch 1 and Chainpur Ch 1 respectively. ***b***, ***d*** show abundances of Al, Ti in Leoville CAI 1. ***c***, ***e***, ***f***, ***h***, ***j***, ***l***, ***p*** show false coloured mosaic images where the colours of abundance of elements are indicated at the bottom of the panel. Scale bars are also shown at the bottom of the panels. The small yellow box at the bottom of panel ***a*** is showing a small region of Wark-Lovering rim as an enlarged view in ***e*** and ***f***. ***n*** shows enlarged BSE image of the inset region of Semarkona Ch 1 shown in ***m***.

shown in Figure 1 by lines 2 and 3 respectively. The composition of the core of melilite is gehlenitic (Åk ~35 wt%) and varies to akermanitic (Åk ~65 wt%) towards the periphery. The outermost ~100 µm show a reversal in a pattern where akermanitic composition of Åk ~65% grades to Åk ~20% typical of Wark-Lovering (WL)-rims. Melilites show $Na_2O$ abundance of ~0.1–0.2%. A small fraction of spinel, pyroxene and anorthite, which are completely enclosed within melilite, are typically not only smaller in size but also lack clear cleavage planes. Idiomorphic to hypidiomorphic granular spinels in size range from a few µm up to ~150 µm are heterogeneously distributed in clusters within the CAI. Spinels are present in two settings: (1) Most of the spinels are either enclosed within anorthite or are at the edges of anorthite within the adjacent pyroxene; (Figure 1 *a* and *c*); (2) Less frequently, but still quite a few numbers of spinel are present within the melilite. The spinel within anorthite and pyroxene are typically in clusters of a large number of spinel grains. The largest spinel in the clusters often twin with one or more spinel. Spinels within the CAIs are mostly Mg-end members, but spinels in the WL-rim have FeO abundance up to ~10 wt%. Spinel and other minerals present in the WL-rim are described separately in the later sections.

Sub-ophitic anorthites are mostly tubular and less frequently angular, with mainly linear contact with melilite. Anorthite is typically 200–300 µm long, ranging from a few µm to ~500 µm. Anorthites hosted completely within melilite in the central part of CAI have mostly free-flowing shapes. The anorthite grains are rather homogeneous in composition and have 98–99% anorthitic component of

**Table 1.** Composition of mineral phases in Leoville CAIs

| Sample | $Na_2O$ | $SiO_2$ | MgO | $Al_2O_3$ | CaO | $TiO_2$ | $Cr_2O_3$ | FeO | Total | Mineral phase | Akermanite (mol.%) |
|---|---|---|---|---|---|---|---|---|---|---|---|
| Leoville CAI 1 | | | | | | | | | | | |
| Interior | 0.1 | 29.9 | 5.3 | 24.0 | 40.8 | 0.0 | 0.0 | 0.0 | 100.0 | Melilite | 35.4 |
| | 0.1 | 34.1 | 8.1 | 16.6 | 40.6 | 0.0 | 0.0 | 0.0 | 99.5 | Melilite | 55.4 |
| | 0.2 | 36.5 | 9.7 | 12.9 | 40.5 | 0.0 | 0.0 | 0.0 | 99.8 | Melilite | 65.5 |
| | 0.1 | 43.3 | 0.1 | 37.4 | 20.0 | 0.1 | 0.0 | 0.0 | 100.9 | Anorthite | |
| | 0.1 | 43.3 | 0.2 | 37.0 | 20.1 | 0.1 | 0.0 | 0.0 | 100.8 | Anorthite | |
| | 0.1 | 43.4 | 0.1 | 37.1 | 19.9 | 0.0 | 0.0 | 0.0 | 100.7 | Anorthite | |
| | 0.1 | 43.2 | 0.2 | 37.2 | 20.0 | 0.1 | 0.0 | 0.0 | 100.8 | Anorthite | |
| | 0.0 | 44.5 | 12.7 | 14.3 | 25.1 | 4.1 | 0.1 | 0.0 | 100.7 | Ca-Pyroxene | |
| | 0.0 | 43.8 | 12.1 | 15.7 | 25.1 | 3.7 | 0.1 | 0.1 | 100.7 | Ca-Pyroxene | |
| | 0.0 | 43.5 | 11.9 | 15.6 | 25.2 | 4.1 | 0.1 | 0.0 | 100.3 | Ca-Pyroxene | |
| | 0.0 | 40.0 | 9.9 | 20.0 | 25.2 | 5.2 | 0.1 | 0.0 | 100.4 | Ca-Pyroxene | |
| | 0.0 | 0.0 | 28.8 | 72.4 | 0.1 | 0.3 | 0.4 | 0.1 | 102.1 | Spinel | |
| | 0.0 | 0.0 | 28.7 | 72.4 | 0.1 | 0.3 | 0.3 | 0.1 | 102.1 | Spinel | |
| | 0.0 | 0.0 | 28.5 | 71.9 | 0.2 | 0.1 | 0.3 | 0.0 | 101.1 | Spinel | |
| | 0.0 | 32.7 | 7.2 | 19.1 | 40.6 | 0.0 | 0.0 | 0.0 | 99.6 | Melilite | 48.8 |
| Rim | 0.1 | 26.7 | 3.5 | 28.5 | 40.2 | 0.0 | 0.0 | 0.3 | 99.2 | Melilite | 23.5 |
| | 0.0 | 39.8 | 8.3 | 21.5 | 27.2 | 1.2 | 0.0 | 0.7 | 98.8 | Ca-Pyroxene | |
| | 0.0 | 52.3 | 16.4 | 5.2 | 23.8 | 0.3 | 0.0 | 1.1 | 99.0 | Ca-Pyroxene | |
| | 0.0 | 41.2 | 48.2 | 0.4 | 1.2 | 0.0 | 0.2 | 8.9 | 100.3 | Olivine | |
| | 0.0 | 43.4 | 51.8 | 0.3 | 2.8 | 0.0 | 0.1 | 3.2 | 101.9 | Olivine | |
| | 0.0 | 44.0 | 43.4 | 2.0 | 4.2 | 0.1 | 0.1 | 6.2 | 100.1 | Olivine | |
| Leoville CAI 3 | | | | | | | | | | | |
| Interior | 0.0 | 23.9 | 1.4 | 34.8 | 38.4 | 0.0 | 0.0 | 0.8 | 99.4 | Melilite | 6.5 |
| | 0.0 | 24.1 | 1.4 | 35.3 | 38.4 | 0.0 | 0.0 | 0.8 | 100.1 | Melilite | 5.3 |
| | 0.0 | 24.6 | 2.0 | 32.2 | 39.7 | 0.0 | 0.0 | 0.4 | 99.0 | Melilite | 13.4 |
| | 0.0 | 23.1 | 1.1 | 34.7 | 39.5 | 0.0 | 0.0 | 0.4 | 98.8 | Melilite | 6.8 |
| | 0.1 | 33.7 | 8.2 | 22.6 | 21.6 | 8.1 | 0.1 | 3.2 | 97.7 | Ca-Pyroxene | |
| | 0.0 | 42.7 | 12.3 | 15.5 | 22.8 | 4.6 | 0.1 | 1.5 | 99.6 | Ca-Pyroxene | |
| | 0.0 | 50.7 | 15.9 | 6.4 | 23.8 | 1.1 | 0.1 | 1.4 | 99.5 | Ca-Pyroxene | |
| | 0.0 | 0.1 | 28.3 | 71.4 | 0.1 | 0.2 | 0.3 | 0.5 | 101.0 | Spinel | |
| | 0.0 | 0.1 | 28.6 | 71.3 | 0.1 | 0.2 | 0.3 | 0.5 | 101.1 | Spinel | |
| | 0.0 | 0.2 | 28.4 | 70.6 | 0.3 | 0.3 | 0.2 | 0.4 | 100.4 | Spinel | |

feldspar (feldspar solid solution (Or–Ab–An)) composition with low $Na_2O$ abundance (<0.12 wt% Table 1). Pyroxenes also show a range of sizes of up to 300 μm. Almost all are associated with anorthite and typically fill the space between anorthite and melilite. The evolving composition of the melt was documented in the large pyroxene grains that showed elemental abundance grading in aluminium and titanium. In general, the pyroxene grains located close to the periphery of the CAIs, show higher abundances of aluminium and titanium and low silica (Figure 1 *a–d*). A reverse pattern is seen for the pyroxenes located in the central region of the CAI. The diopside in the CAI was aluminium-rich ($Al_2O_3$ up to ~20%; typical ~13%). $TiO_2$ abundance in them ranged up to 7 wt%. The composition of the diopside in WL-rim was different.

A WL-rim of ~100 μm width palisades half of the exposed perimeter of the CAI; the other half is a broken fragmental remains (Figure 1 *e* and *f*). At a few places, the WL-rim intruded into the melilite layer, forming doubly repetitive WL-rims (Figure 1 *a* line 4; Figure 2 *b* and *c*). The WL-rim comprises spinel, hibonite (rare), melilite, anorthite, pyroxene and olivine rims sequentially from inside to outside. Hibonites are small and rare, and perovskites are very rare. The melilite in the WL-rim was more silicon and aluminium rich than melilite, located more than a few 100 μm away from the WL-rim. A typical variation is shown by line 3 in Figure 1 where the melilite composition varies from Åk ~55 wt% to Åk ~20 wt% at the base of the spinel-hibonite layer. Spinels in the WL-rim are generally small, up to ~50 μm in size, with the majority being in the range of 5–10 μm. They contain variable amounts of FeO from a few wt% up to ~10 wt%. The anorthite rim was discontinuous and only a few μm in width. Melilite layer often present in the WL-rim was between spinel ± hibonite ± perovskite layer, and anorthite layer was not very well demarcated as the basal spinel layer was not continuous in this CAI. Outside the anorthite rim is a pyroxene (diopside) rim of ~15–20 μm in width. The pyroxene rim showed a gradient of titanium-rich pyroxene to aluminium-rich pyroxene outwards (Figure 1 *f*). The overlying forsteritic (Mg-rich) olivine layer was also discontinuous with a variable thickness of up to ~60 μm. An accretionary rim consisting of fine-grained (1–2 μm) fayalitic material was present in some of the depressional edges of the CAIs.

Leoville CAI 3 is an elongated, irregularly shaped melilite-rich fluffy Type A CAI of ~500 μm in size (Figure 1 *g*

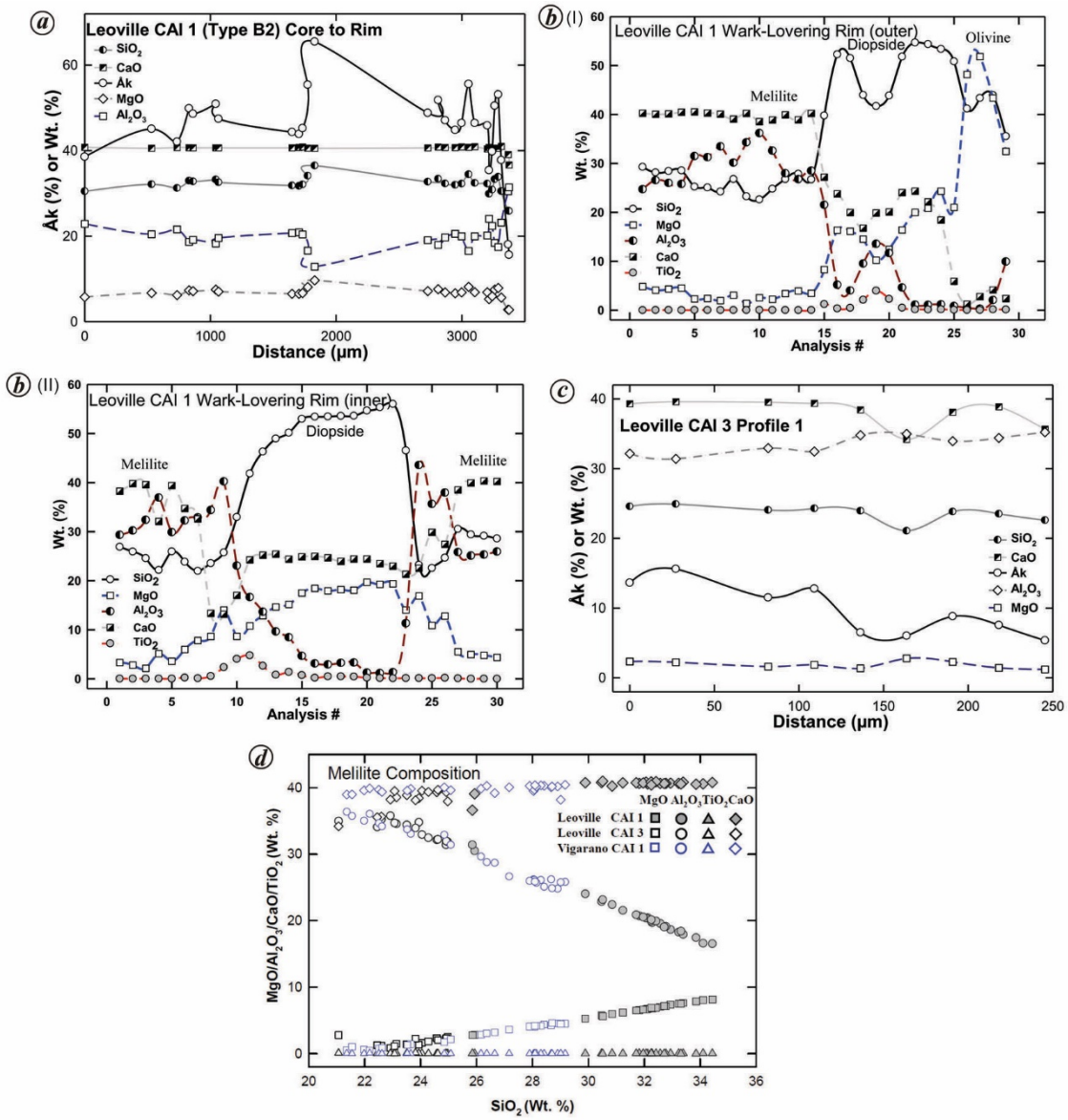


**Figure 2.** ***a***, Variation of elemental oxides with distance measured from a fixed point in the centre of Leoville CAI 1. ***b***, Variation of elemental oxides along line 4 (see Figure 1 and text) in the outer (I) and inner (II) Wark-Lovering rim of Leoville CAI 1 from the region where double Wark-Lovering rim is present. Note the presence of melilite at the start and end of the profile in the inner (II) rim. ***c***, Variation of elemental oxides with distance measured from a fixed point in the centre of Leoville CAI 3. ***d***, Comparison of major elemental oxides in melilites of Leoville CAI 1 (Type B2), Leoville CAI 3 (Type A) and Vigarano CAI 1 (Type A) (see text for details).

and *h*). Several nodules with similar morphological and mineralogical characteristics but varying sizes seemed mildly sintered to constitute this CAI. Usually, a nodule consists of a melilite core surrounded by a thin rind of anorthite. A thick titanium-rich pyroxene layer envelopes it. Most nodules have sub-μm to μm sized spinel and perovskite, in one case two large grains (~30 μm), in the core of the nodules. A linear profile in melilite (line 1 in Figure 1 *g*) in the CAI showed a narrow range of gehlenitic (Åk 6–13) composition (Figures 1 *g*, *h*, 2 *d*, *e*; Table 1). Normal abundances of $Al_2O_3$ and MgO in melilite are ~33 and 1.5 wt% respectively. Spinels are primarily Mg-end members with FeO abundances of ~1.0 wt%. Diopside (Ca-pyroxene) has $TiO_2$ abundances <2.0 wt%. A few cross-cutting Fe-veins of varying thickness (5–35 μm) passed through the CAI. The other large (~150 × 50 μm sized) fragmental CAI identified about 600 μm away was separated by a chondrule between the CAIs. It was likely that the fragmental remains of CAI 3 were similar to other smaller two–three pieces of CAI in the neighbourhood. The two thicker Fe-rich veins would have most likely metamorphosed ~70 and 30 μm wide zone at the vein contact. The altered regions were richer in iron, aluminium and silicon, which seem to have replaced calcium, and titanium in compacted clay. Regions around the veins were distinctly enriched in aluminium and passed across the neighbouring chondrule.

Semarkona (LL3.00), a 0.691 kg meteorite 'fall' from Semarkona, Madhya Pradesh, India, is classified as an ordinary chondrite with very low iron abundance belonging to petrographic type ~3.00 (refs 5, 6). CAIs and refractory inclusions are extremely rare. The limited few found so far are typically small (<200 μm)[12–20]. An anomalously large porphyritic, pyroxene type IB (Type 1 has FeO < 10 wt%; B indicates predominance of pyroxene mineral phases while A indicates predominance of olivine) chondrule Ch# 27 (Figure 1 *m*) was selected for the present study. Generally, Type I chondrules, which are Mg-rich and Fe-poor, are rare in ordinary chondrites, but are the dominant type in the carbonaceous chondrites. Semarkona Ch# 27 is circular in shape with a diameter of 3 mm (Figure 1 *m*). In the three thin sections of Semarkona chondrite (9337 PRL (area 123 $mm^2$), 4128-5 AMNH (164 $mm^2$); t4-ps-7b AMNH (93.4 $mm^2$)) for a total approximate area of ~380.4 $mm^2$, only one other chondrule (porphyritic pyroxene) of such large dimension was observed. This mega chondrule is twice the size of typical chondrules in Semarkona[21–26]. The thin section containing the mega chondrule had about 100 smaller chondrules, of which 6 (barred olivine Ch# 39, 47; barred olivine pyroxene Ch# 43, 48; barred pyroxene Ch# 37; excentro-radial Ch# 40) have non-porphyritic morphology with similarities[24] to Ch# 27. It consisted of pyroxene bars which were mostly aligned in one particular direction. The pyroxene grains at the edges are smaller (less than half the length of centrally located pyroxene) and oriented perpendicular to the centrally located pyroxene bars. Some of the pyroxenes had small (2–5 μm) overgrowths of Ca-rich (pyroxene like? unidentified) phase. The mesostasis between the pyroxene crystals was glassy and predominantly free of Mg-rich microcrystallites normally seen in porphyritic chondrules in Semarkona. Spherical Fe- (Ni rare <2% abundance) metal and sulphide blebs of a few μm up to ~60 μm (2/188) were present within the chondrule. Most of the metal grains are located within the mesostasis, and only a few (<5% by number) are within the pyroxene grains. A similar distribution of metal and metal sulphide grains was observed in non-porphyritic chondrules in Semarkona, particularly in Ch# 39 (barred olivine) and Ch# 40 (excentro-radial) which have been previously studied in $^{26}Al$–$^{26}Mg$ and $^{60}Fe$–$^{60}Ni$ isotopic studies[16,24,27], and are located proximally to Ch# 27. Two–three large metal grains (10–20 μm) showed a juxtaposition of Fe, Ni and FeS within the grains, which is suggestive of a lack of any thermal metamorphism after the formation of this chondrule. The distribution of FeS in conjunction with Fe, Ni metals is also supportive of the low degree of alteration. The chondrule was surrounded by a thick rim of FeS, typical of several other chondrules in Semarkona and other unequilibrated ordinary chondrites.

An 8.2 kg meteorite which fell in 1907 at Chainpur, Uttar Pradesh, India, belongs to the ordinary chondrites of LL type. It was classified as petrographic type 3.4 Chainpur (LL3.4) is a 8.2 kg meteorite. The Al-rich chondrule was ~200 μm in diameter (Figure 1 *o*). Al-rich chondrules in unequilibrated ordinary chondrites constitute less than 2% by number abundance but are of significant interest owing to their suitability for $^{26}Al$–$^{26}Mg$ isotope systematics. They primarily comprise olivine, plagioclase, pyroxene and Fe–Ni metal. The fragmented peripheral morphology of the chondrule makes its classification difficult, but the presence of large laths of plagioclase enables it to be classified as plagioclase pyric type of Al-rich chondrule[28]. The outer boundary of the chondrule was fractured and broken, with uneven remains of the peripheral grains, unlike the typical distinct circular boundary observed in chondrules from low petrographic type (~3.0–3.3). Two large (~50–100 μm) metal (Fe, Ni, Cr, P) nodules were also present, along with a few Fe–Ni veins cutting across the chondrule. The chondrule was surrounded by fine-grained fayalite and small metal sulphide grains. A rare occurrence of a large CAI (partially seen in Figure 1 *o* and *p*) in close proximity is another notable feature.

Queen Alexandra range (QUE) 99177 (CR3.00) is a 43.6 g meteorite 'find' from Antarctica collected by ANSMET (ANtarctic Search for METeorites) expedition in 1999. It has been classified[29] as CR3.00. Two chondrules from the meteorite were selected for the study.

Chondrule 1 (Ch# 1, Figure 1 *i* and *j*) was a porphyritic pyroxene spherical chondrule of ~450 μm diameter. It consisted predominantly of pyroxene with a few bar-shaped olivine phenocrysts. The olivine bars were surrounded by Al-rich glassy phases. A thin circular band of olivine (2 μm) surrounded at least half the perimeter of the chondrule that was indistinguishable from the surrounding pyroxene in the BSE image. The chondrule was free of metal grains, but a few metal – sulphide grains were at the outer edge of the chondrule.

Chondrule 2 (Ch# 2, Figure 1 *k* and *l*) was a barred olivine chondrule that was a fragmental remain of the size 700 × 600 μm. It was a rare IIA (FeO rich >10 wt.%; olivine dominated) type chondrule in the CR chondrite, where typically Type I chondrules are present. The chondrule hosted a few grains of chromite, Fe and Ni. The olivine bars were surrounded by glassy mesostasis. A thin rim of fine-grained Ca-rich mineral dust surrounded the chondrules.

## Results of Al and Mg isotopic studies

The results of $^{26}Al$–$^{26}Mg$ isotopic studies in a few CAIs and chondrules from unequilibrated chondrites are presented in Tables 2 and 3 and shown in Figure 2. A range of radiogenic excess in the $\Delta^{26}Mg$ up to 80‰ was observed in Leoville CAIs. Chondrules, on the other hand, mostly yielded unresolved radiogenic excess in $\Delta^{26}Mg$. The radiogenic excess in $^{26}Mg/^{24}Mg$ ratios in melilite and anorthite within Leoville CAI 1 correlated with their corresponding $^{27}Al/^{24}Mg$ ratios. An error-weighted linear regression of the data yielded an isochron that corresponded to $^{26}Al/^{27}Al$ of $(4.84 \pm 0.31) \times 10^{-5}$ with an intercept of $1.2 \pm 0.5$‰. The melilites

**Table 2.** $^{26}Al$–$^{26}Mg$ isotopic data

| Analysed object | Analysed phase | $^{27}Al/^{24}Mg$ | $2\sigma$ | $\Delta^{26}Mg$ | $2\sigma$ | $\delta^{25}Mg$ | $2\sigma$ | $\delta^{26}Mg$ | $2\sigma$ |
|---|---|---|---|---|---|---|---|---|---|
| 12March-Leoville-CAI1-An-1 | Anorthite | 186.1 | 18.6 | 60.9 | 5.3 | 3.9 | 2.3 | 68.5 | 2.9 |
| 12March-Leoville-CAI1-An-1-1 | Anorthite | 188.7 | 18.9 | 67.8 | 5.0 | 1.8 | 2.4 | 71.3 | 2.9 |
| 12March-Leoville-CAI1-An-1-2 | Anorthite | 190.6 | 19.1 | 70.6 | 5.5 | 2.4 | 2.4 | 75.2 | 3.5 |
| 12March-Leoville-CAI1-An-1-3 | Anorthite | 189.3 | 18.9 | 67.2 | 5.7 | 3.6 | 2.4 | 74.3 | 3.2 |
| 12March-Leoville-CAI1-Mel-1 | Melilite | 2.2 | 0.2 | 2.3 | 1.0 | 0.7 | 0.5 | 3.6 | 0.8 |
| 12March-Leoville-CAI1-Mel1-1-1 | Melilite | 1.9 | 0.2 | 1.6 | 1.0 | –1.0 | 0.4 | –0.4 | 0.5 |
| 12March-Leoville-CAI1-Mel-1-2 | Melilite | 1.9 | 0.2 | 1.6 | 1.0 | –1.4 | 0.4 | –1.1 | 0.5 |
| 12March-Leoville-CAI1-Mel-1-3 | Melilite | 1.9 | 0.2 | 2.2 | 1.1 | –2.0 | 0.5 | –1.7 | 0.8 |
| 11March17-Leoville-CAI3-1 | Melilite + Px | 2.8 | 0.3 | 1.5 | 0.9 | –5.1 | 0.4 | –8.5 | 0.6 |
| 11March17-Leoville-CAI3-1-1 | Melilite + Px | 2.7 | 0.3 | 1.5 | 0.8 | –6.2 | 0.4 | –10.5 | 0.5 |
| 11March-Leoville-CAI3-1-2 | Melilite + Px | 2.6 | 0.3 | 2.0 | 0.9 | –7.1 | 0.3 | –11.8 | 0.5 |
| 11March17-Leoville-CAI3-2 | Melilite | 7.6 | 0.8 | 1.7 | 1.5 | –3.7 | 0.7 | –5.5 | 0.7 |
| 11March17-Leoville-CAI3-2-1 | Melilite | 7.0 | 0.7 | 3.7 | 1.5 | –6.5 | 0.9 | –9.0 | 1.1 |
| 11March-Leoville-CAI3-2-2 | Melilite | 6.7 | 0.7 | 2.3 | 1.4 | –6.3 | 0.6 | –10.0 | 0.8 |
| 11March17-Leoville-CAI3-3 | Al-rich altered | 1.1 | 0.1 | 3.0 | 0.6 | –5.5 | 0.4 | –7.6 | 0.5 |
| 11March17-Leoville-CAI3-3-1 | Al-rich altered | 1.0 | 0.1 | 2.7 | 0.7 | –7.6 | 0.3 | –12.0 | 0.4 |
| 11March17-Leoville-CAI3-3-2 | Al-rich altered | 1.0 | 0.1 | 3.0 | 0.6 | –8.1 | 0.3 | –12.8 | 0.3 |
| 11March17-Leoville-CAI3-3-3 | Al-rich altered | 1.1 | 0.1 | 2.5 | 1.0 | –8.1 | 0.3 | –13.2 | 0.8 |
| 11March17-Leoville-CAI3-4 | Al-rich altered | 4.1 | 0.4 | –0.4 | 0.8 | –3.0 | 0.4 | –6.2 | 0.6 |
| 11March17-Leoville-CAI3-4-1 | Al-rich altered | 3.5 | 0.3 | 0.4 | 0.7 | –4.8 | 0.3 | –9.0 | 0.5 |
| QUE 99177Ch1meso-1 | Pyroxene | 1.2 | 0.1 | –0.3 | 1.0 | –10.5 | 0.5 | –20.7 | 0.6 |
| QUE 99177Ch1meso-1-1 | Pyroxene | 1.1 | 0.1 | –0.1 | 1.0 | –11.1 | 0.5 | –21.6 | 0.6 |
| QUE 99177Ch1meso-1-2 | Pyroxene | 1.0 | 0.1 | –0.8 | 1.0 | –9.7 | 0.5 | –19.6 | 0.6 |
| QUE 99177Ch1meso-1-3 | Pyroxene | 1.0 | 0.1 | –0.5 | 1.0 | –9.2 | 0.4 | –18.4 | 0.5 |
| QUE 99177Ch1meso-2 | Pyroxene | 1.3 | 0.1 | –0.4 | 1.4 | –7.8 | 0.7 | –15.6 | 0.9 |
| QUE 99177Ch1meso-2-1 | Pyroxene | 1.0 | 0.1 | –0.7 | 1.0 | –7.1 | 0.4 | –14.5 | 0.6 |
| QUE 99177Ch1meso-2-2 | Pyroxene | 0.9 | 0.1 | –0.5 | 0.8 | –7.5 | 0.4 | –15.0 | 0.5 |
| QUE 99177Ch1meso-2-3 | Pyroxene | 0.9 | 0.1 | –0.4 | 0.8 | –7.2 | 0.4 | –14.4 | 0.5 |
| QUE 99177Ch1meso-3 | Pyroxene | 1.0 | 0.1 | 0.0 | 0.9 | –5.8 | 0.4 | –11.2 | 0.7 |
| QUE 99177Ch1meso-3-1 | Pyroxene | 0.8 | 0.1 | 0.0 | 0.8 | –5.7 | 0.4 | –11.1 | 0.4 |
| QUE 99177Ch1meso-3-2 | Pyroxene | 0.8 | 0.1 | 0.3 | 0.8 | –6.0 | 0.3 | –11.4 | 0.4 |
| QUE 99177Ch1meso-3-3 | Pyroxene | 0.8 | 0.1 | 0.6 | 0.7 | –6.3 | 0.3 | –11.6 | 0.4 |
| QUE 99177Ch1meso-4 | Pyroxene | 1.0 | 0.1 | –0.2 | 1.0 | –5.8 | 0.5 | –11.4 | 0.8 |
| QUE 99177Ch1meso-4-1 | Pyroxene | 0.7 | 0.1 | 0.2 | 1.0 | –5.5 | 0.4 | –10.4 | 0.4 |
| QUE 99177Ch1meso-4-2 | Pyroxene | 0.7 | 0.1 | –0.4 | 0.8 | –5.6 | 0.4 | –11.3 | 0.5 |
| QUE 99177Ch1meso-4-3 | Pyroxene | 0.7 | 0.1 | –0.4 | 0.8 | –5.7 | 0.4 | –11.5 | 0.4 |
| QUE 99177Ch2meso-1 | Glass | 4.8 | 0.5 | –2.3 | 1.3 | –2.9 | 0.8 | –8.0 | 1.1 |
| QUE 99177Ch2meso-1shift-1 | Glass | 22.1 | 2.2 | –0.8 | 2.3 | –2.7 | 1.1 | –6.1 | 1.4 |
| QUE 99177Ch2meso-1shift-1-1 | Glass | 20.0 | 2.0 | –0.7 | 2.4 | –2.0 | 1.1 | –4.7 | 1.4 |
| QUE 99177Ch2meso-1shift-2 | Glass | 20.4 | 2.0 | –0.6 | 2.4 | –2.0 | 1.1 | –4.5 | 1.3 |
| QUE 99177Ch2meso-2 | Glass | 37.7 | 3.8 | 0.8 | 3.4 | –5.3 | 1.6 | –9.5 | 2.3 |
| QUE 99177Ch2meso-3 | Glass | 33.1 | 3.3 | –0.6 | 3.1 | –1.7 | 1.3 | –3.8 | 1.5 |
| QUE 99177Ch2meso-1 | Glass | 5.7 | 0.6 | –1.2 | 1.3 | –3.7 | 0.6 | –8.4 | 0.8 |
| 11March-SemarkonaCh27-1 | Glass | 7.4 | 0.7 | 1.0 | 1.6 | –2.2 | 0.8 | –3.2 | 1.2 |
| 11March-SemarkonaCh27-1-1 | Glass | 6.2 | 0.6 | 1.6 | 1.1 | –2.3 | 0.5 | –3.0 | 0.7 |
| 11March-SemarkonaCh27-2 | Glass | 11.1 | 1.4 | –1.4 | 4.9 | –5.5 | 1.9 | –12.1 | 3.5 |
| 11March-SemarkonaCh27-2-1 | Glass | 8.0 | 0.8 | 1.1 | 1.3 | –1.4 | 0.6 | –1.6 | 0.8 |
| 11March-SemarkonaCh27-3 | Glass | 8.8 | 0.9 | –0.8 | 2.1 | –3.3 | 1.3 | –7.3 | 1.9 |
| 11March-SemarkonaCh27-3-1 | Glass | 6.7 | 0.7 | 1.1 | 1.2 | –2.0 | 0.6 | –2.7 | 0.8 |
| 10March17-Chainpur-Ch1-plag-1 | Plagioclase | 3.1 | 0.3 | 1.0 | 0.6 | –2.9 | 0.3 | –4.7 | 0.5 |
| 10March17-Chainpur-Ch1-plag-1-1 | Plagioclase | 2.2 | 0.2 | 1.7 | 0.4 | –5.2 | 0.2 | –8.3 | 0.3 |
| 10March17-Chainpur-Ch1-plag-2 | Plagioclase | 34.1 | 3.4 | –1.9 | 2.4 | 0.5 | 1.0 | –0.9 | 1.3 |
| 10March17-Chainpur-Ch1-plag-2-1 | Plagioclase | 34.6 | 3.5 | –1.5 | 2.5 | –1.4 | 1.1 | –4.2 | 1.3 |
| 10March17-Chainpur-Ch1-plag-2-2 | Plagioclase | 34.0 | 3.4 | 1.4 | 2.1 | –3.3 | 1.1 | –5.1 | 1.2 |
| 10March17-Chainpur-Ch1-plag-3 | Plagioclase | 32.1 | 3.2 | –1.4 | 2.2 | 0.5 | 1.0 | –0.3 | 1.3 |
| 10March17-Chainpur-Ch1-plag-3-1 | Plagioclase | 34.2 | 3.4 | 0.6 | 2.2 | –2.4 | 1.0 | –4.1 | 1.3 |
| 10March17-Chainpur-Ch1-plag-3-2 | Plagioclase | 33.6 | 3.4 | 1.8 | 2.5 | –3.2 | 1.0 | –4.5 | 1.3 |

present in Leoville CAI 3 were rather uniform and spanned a limited range of Åkermanite (6–13). Analysis within the melilite yielded a limited range of $^{27}Al/^{24}Mg$, but well-resolved excesses in $^{26}Mg/^{24}Mg$ were observed. However, due to a limited range of low $^{27}Al/^{24}Mg$ (<10), the regression through the data yielded an isochron corresponding to $^{26}Al/^{27}Al$ of $(2.8 \pm 3.1) \times 10^{-5}$. A few analyses on two additional spots in the Al-rich region (indicated as a circle with

**Table 3.** Results of $^{26}Al$–$^{26}Mg$ isotope systematics

| Object | $^{26}Al/^{27}Al$ | $2\sigma$ | Intercept | $2\sigma$ | MSWD | Probability | $\Delta^{26}Mg_0$ | $2\sigma$ |
|---|---|---|---|---|---|---|---|---|
| Leoville CAI 1 | 4.84E-05 | 3.10E-06 | 0.13949 | 0.00007 | 0.6 | 0.8 | 1.2 | 0.5 |
| Leoville CAI 3 Selected | 2.77E-05 | 3.05E-05 | 0.13947 | 0.00013 | 1.3 | 0.3 | 1.1 | 0.9 |
| Leoville CAI 3 All | -4.71E-05 | 5.70E-05 | 0.13971 | 0.00017 | 6.9 | 0.0 | 2.8 | 1.2 |
| QUE 99177 Ch2 | 8.65E-06 | 9.60E-06 | 0.13904 | 0.00015 | 0.3 | 0.9 | –2.0 | 1.1 |
| Semarkona Ch27 | -8.51E-05 | 9.20E-05 | 0.14007 | 0.00067 | 0.4 | 0.9 | 5.4 | 4.8 |
| Chainpur Ch 1 | -7.45E-06 | 8.20E-06 | 0.13955 | 0.00010 | 2.2 | 0.4 | 1.6 | 0.7 |

broken lines) were also made. One of the regions with low $^{27}Al/^{24}Mg$ yielded high $^{26}Mg/^{24}Mg$ ratios, while the other yielded lower unresolved values. Analyses from these two spots were not considered for the calculation of the isochron. If analyses from these two regions are also considered, then an isochron with a negative slope corresponding to $^{26}Al/^{27}Al$ value of $-(4.7 \pm 5.7) \times 10^{-5}$ would be obtained.

Al–Mg isotopic studies were also carried out in a mega chondrule from Semarkona and a plagioclase-rich chondrule from Chainpur. The clear glassy mesostasis regions of Semarkona Ch 27 had a low and narrow range of $^{27}Al/^{24}Mg$ ratio that did not help in determining its time of formation. The plagioclase in the Chainpur chondrule gave a reasonable range of Al/Mg (~40), but some regions of plagioclase inferred from the isotopic data seemed to have a disturbed isotopic ratio that was discordant with other data obtained from the chondrule. Hence, this chondrule also did not yield a resolved isochron by weighted regression of all the data. However, a few data points were resolved from the chondritic value, and a few others were, in general, consistent with the typical $^{26}Al/^{27}Al$ ratio of $\leq 1 \times 10^{-5}$ of chondrules from unequilibrated ordinary chondrites[30].

Two chondrules from unequilibrated carbonaceous chondrite QUE 99177 (CR3.00) were analysed. The data obtained from these chondrules (Table 2) is shown in Figure 3 *c*. The glassy mesostasis in QUE 99177 Ch# 1 yielded very low $^{27}Al/^{24}Mg$ ratios, and the measured $^{26}Mg/^{24}Mg$ were unresolved from the chondritic value (0.13932) which did not yield a resolved $^{26}Al$ isochron. The Type II barred chondrule in QUE 99177 showed a marginally larger range of $^{27}Al/^{24}Mg$ up to ~40. Due to the lower abundance of Mg in these phases, large error bars of the measurement yielded an unresolved isochron.

## Discussion

### *Formation of Leoville CAI 1*

The petrogenetic history of the CAI can be constrained by petrography, mineralogy, size and composition of minerals and mineral associations criteria. The timing of these events can be constrained from the relative chronometer (e.g. $^{26}Al$), anchored to an absolutely dated event or object. Dynamic crystallization experiments for a Type B bulk CAI composition for a set of a range of maximum temperature ($T_{max}$ 1580–1275°C) from above liquidus to solidus for a range of time duration (16.5–0.83 h) at the maximum temperature ($T_{max}$) and cooling rates (0.5–1000°C/h) were carried out to understand crystallization sequence of minerals and the resulting morphology and mineralogy of the formed mineral phases[31–33].

Several petrographic observations described in the previous sections (meteorites and analysed objects) suggest the formation of Leoville CAI 1 from a partial (Type B composition) melt heated to a maximum temperature of ~1420°C for a short duration. The large grain sizes suggest a slow cooling rate of ≤0.5°C/h in a physically unconstrained space[31]. Melilites are normally zoned with gehlenitic core and increasing akermanitic composition outwards. A typical pattern in a blocky melilite is indicated (short line, line 2) in Figure 1 *a*. The cores of melilite grains become increasingly akermanitic towards the periphery (Figure 2 *a*). The akermanitic composition of melilite ranged from ~35 in the inner regions to ~65 wt.% in the outer regions of the CAIs. Reverse zoning and/or oscillatory zoning in the periphery was also observed in a few large grains in the centre (Figure 1). Note the significant variation in abundances of Al (Figure 1 *b*) in the rims of melilite phases located in the central region of the CAI which show reverse and/or oscillatory zoning. A few large melilite grains in the centre also show a normally zoned core, overgrown by a reversely zoned rim. The slow cooling rate assisted in the formation of large grains of melilite and spinel. Heterogeneous distribution of spinel nucleating sites resulted in the formation of spinel grains with a large range of sizes and geometrical arrangement (linear to circular). Most of the spinel grains forming and growing along with melilite were eventually nudged out of the melilite grains. On cooling to temperatures of ~1250°C, Ca-rich pyroxene began to crystallize first, which resulted in the reverse-zoned growth of melilites present in the central regions of the CAI. Plagioclase began to crystallize shortly after and continued to crystallize at a slow cooling rate leading to the formation of large equant grains of laths of anorthite and pyroxene. The aluminium, titanium-rich overgrowth of pyroxene indicates that during the terminal phase, only pyroxene continued to crystallize without further addition/growth of plagioclase. At the end of crystallization, a large Type B CAI was the end product. Initially formed, larger CAI was subsequently evaporated at the periphery to form the WL-rim. The zoning in Al, Mg, Si almost up to a distance of ~100 μm from the WL-rim

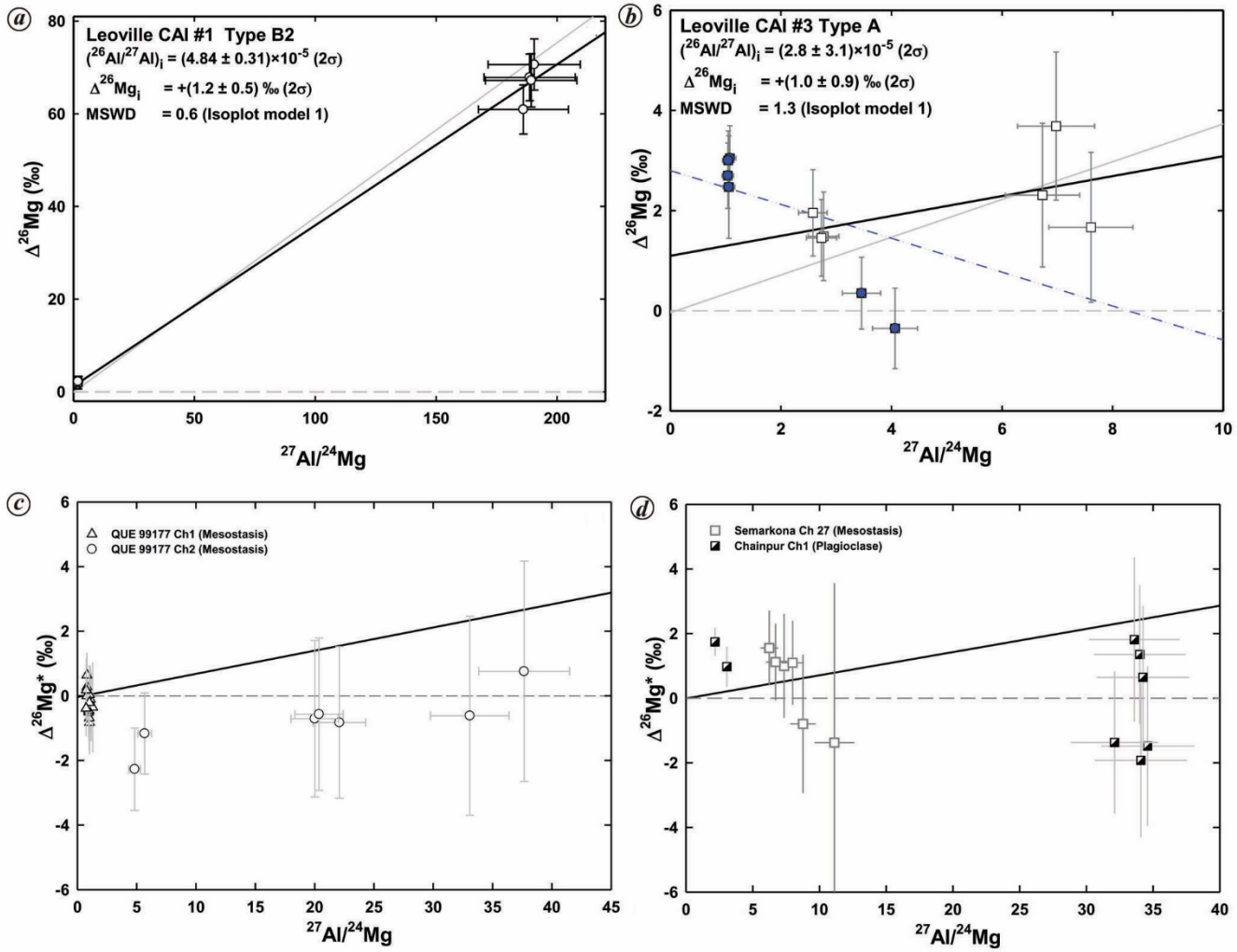


**Figure 3.** $^{26}$Al–$^{26}$Mg isotopic diagram. (***a***) $^{26}$Al–$^{26}$Mg isotopic diagram for Leoville CAI 1. The dark black line is the linear regression line obtained from the data. The 2$\sigma$ errors of the regression line and intercept are also shown in the panel. The errors associated with the data are 2$\sigma$. The horizontal broken line shows the chondritic ratio while the light grey line is the canonical abundance line that corresponds to $^{26}Al/^{27}Al$ of 5.25 × 10$^{-5}$. (***b***) $^{26}$Al–$^{26}$Mg isotopic diagram for Leoville CAI 3. The filled blue colour squares indicate data obtained from the altered phases. The dark black line is the linear regression line obtained from the data shown in white colour. The 2$\sigma$ errors of the regression line and intercept are also shown in the panel. The dash dot (blue coloured) line is the regression line obtained when considering the entire dataset. The errors associated with the data are 2$\sigma$. The horizontal broken line shows the chondritic ratio while the light grey line is the canonical abundance line that corresponds to $^{26}Al/^{27}Al$ of 5.25 × 10$^{-5}$. (***c***) $^{26}$Al–$^{26}$Mg isotopic diagram for analysed chondrules in Queen Alexandra range (QUE) 99177 (CR3.0). The errors associated with the data are 2$\sigma$. The horizontal broken line shows the chondritic ratio while the light grey line corresponds to $^{26}Al/^{27}Al$ of 1.0 × 10$^{-5}$. (***d***) $^{26}$Al–$^{26}$Mg isotopic diagram for analysed chondrules in Semarkona (LL3.00) and Chainpur (LL3.4). The errors associated with the data are 2$\sigma$. The horizontal broken line shows the chondritic ratio while the light grey line corresponds to $^{26}Al/^{27}Al$ of 1.0 × 10$^{-5}$.

suggests short duration evaporation of a few minutes (?) to hours at a temperature of ~1650°C (ref. 31). The absence of significant hibonite, perovskite and anorthite from the WL-rim suggests suppression of crystallization of anorthite under a total pressure of $10^{-3}$ atmospheres and or enrichment of dust by a factor of ~$10^3$ (ref. 33).

### *Hearth and thermal history of large Type B CAIs in CV3*

CV3 chondrites are characterized by a preponderance of large-sized CAIs. The large size of these CAIs has enabled multi-dimensional investigations relating to petrography, mineralogy, multiple stable and radiogenic isotopic studies, evaporation–condensation, etc. These studies have allowed us to deduce cosmo-chemical conditions and chronology of the early solar system events, processes and solids[3,34–41]. A natural consequence of stochastic, highly energetic and rapid cosmo-chemical processes under quasi-dynamic equilibrium state is the plausibility of multiple pathways for an ensemble of early solar system solids, including CAIs. The genesis and thermal evolution of the large CAIs in CV3 demonstrate the multiple pathways phenomenon and are one of the prime causes for the observed diversity amongst these kinds of CAIs[3,40–42]. The formation and crystallization history of the Leoville CAI 1

is distinct from other large Type B CAIs studied previously in Vigarano, Efremovka and other CV3s. A large 6.4 × 4.8 mm fragmental Type B1 Efremovka CAI# 40 studied for $^{26}$Al–$^{26}$Mg and Li–Be–B experienced a similar range of $T_{max}$ of ~1240°C, but the duration of $T_{max}$ must have been prolonged (several hours) to destroy almost all the nucleating sites of anorthite[43,44]. A more extreme and even longer duration of $T_{max}$ must have been experienced by Vigarano CAI 1 (Type A, 4.5 × 3.6 mm), which consists only of melilite and spinel[26]. Leoville CAI 1 has higher similarity in mineralogy, shape and texture to an oval-shaped ~3 × 2 mm Type B1 CAI of Efremovka CAI 3 (EF3). Apart from the difference in the size of the two CAIs, the other major difference with Efremovka CAI 3 is the relatively larger abundance of anorthite and smaller spinel grain that most likely resulted from a shorter duration and/or marginally lower maximum temperature of partial melt[45]. It is also possible that the precursors of CAI (EF3) were preheated at a lower temperature before the more intense thermal events that later finally formed the CAI. It has been shown from dynamic crystallization experiments that low-temperature pre-crystallization facilitates nucleation of anorthite[32].

The range of composition of melilites in Leoville CAI 1, CAI 3 and Vigarano CAI 1 is shown in Figure 2, which, at first order is indicative of their petrogenesis. $^{26}$Al–$^{26}$Mg relative chronometer dating of these large CAIs have yielded $^{26}$Al/$^{27}$Al of $(5.002 \pm 0.064) \times 10^{-5}$, $(4.84 \pm 0.31) \times 10^{-5}$, $(4.89 \pm 0.38) \times 10^{-5}$, $(3.4 \pm 1.0) \times 10^{-5}$ for Leoville 3535-1, Leoville CAI# 1, Vigarano CAI# 1 and Efremovka CAI 40 respectively[40,43,44,46]. The $^{26}$Al/$^{27}$Al abundances in these CAIs suggest their formation at $0.1 \pm 0.08$ Ma respectively, if the canonical value of $5.25 \times 10^{-5}$ of non-igneous CAIs[39] is assumed as starting value. The time of formation suggests their formation contemporaneously at $0.1 \pm 0.08$ Ma, plausibly from the same thermal event with the evolution and cooling rate of each CAI dictated by its local environment.

## *Formation and evolution of Leoville CAI 3*

The morphology and mineralogy of CAI 3 (discussed earlier) are typical of fluffy Type A CAIs that (de)grade with increasing loss of the multi-mineralic layered nodular characteristics towards a single morphological (homogeneous) unit of compact Type A and Type B, and are more explicitly seen in Efremovka CAI 1 (refs 35, 40). The formation of such typical Type A has been previously explained by sequential nucleation/addition of lesser refractory mineral phases on one of the most refractory abundant phases of either/or of spinel ± hibonite ± perovskite by gas–solid crystallization from the solar gas. The Leoville CAI 3, during their compaction into the parent body, was further compacted, morphologically reformed into elongate shapes, and plausibly separated with ¼ portion of the nodules by the compressing chondrules and matrix. Later, within the parent body, fluid-assisted alteration took place locally in the regions where Fe,-S or aqueous alteration took place that was presently seen as veins crossing the CAI. It is, however, noteworthy that the distribution of Na and S is heterogeneous, non-contiguous within the melilite and the nodules. Such an abundance pattern is suggestive that except for the regions affected by hydrothermal and/or Fe, FeS veins, the remaining parts of the CAI are largely unaffected and likely are pristine. The isotopic systematics in the regions affected by hydrothermal and Fe, FeS veins were variably disturbed. The $^{26}$Al/$^{27}$Al obtained by regression through the data reflects this alteration in the isotope systematics. The analyses of regions away from the veins yield an unresolved isochron compatible with the formation of CAI ~1 million years later than the material characterized by the canonical value.

## *Multiple epochs of CAIs' formation*

In the case of homogeneous distribution of short-lived chronometers in the early solar system, a key problem has been to identify the epoch of formation of CAIs and/or distinguish their relationship chemically and temporally with chondrules. High precision $^{26}$Al–$^{26}$Mg isotope systematics in a suite of CAIs from the unequilibrated carbonaceous chondrite of the lowest petrographic type indicated multiple episodes of formation of CAIs that are also characterized by some distinction in the petrography and mineral composition of the CAIs[19,39–41,46]. These large CAIs studied previously and in the current study agree with the aforesaid assertion. Scale and temporal constraints of isotopic homogeneity in the early solar system is currently debated[3,39,40,47–49], but multiple epochs of formation of CAIs and other refractory solids[50,51] are suggested in both scenarios. The $^{26}$Al–$^{26}$Mg isotope systematics in the above-mentioned CAIs suggest an epoch of ~0.1 Ma CAI formation after the time $T_0$ that is characterized by the canonical abundance of $^{26}$Al/$^{27}$Al of ~$5.25 \times 10^{-5}$. It can be inferred that this duration corresponds to one of the major episodes of CAI formation during which the cosmo-chemical conditions enabled the formation of large CAIs that were later accreted into CV chondrites. Finding an answer to the question of the formation of different types of CAIs (fine grained spinel-rich, Type A, B, Cs) in distinct non-overlapping epochs from a homogeneous early solar system has been attempted[19,40,41,46], but the question remains a difficult one which needs to be unequivocally resolved. Additional plausible petrographic and isotopic studies of the CAIs will shed further light and constrain the early evolution of the solar system.

## *Isotopic systematics of chondrules*

Chondrules with apparent special features were selected for the present study to conduct multiple isotope systematics studies. However, none of these objects yielded resolved $^{26}$Al isochrons. In the following, we discuss the formation

and isotopic records of two chondrules which present the most interesting cases.

The unusually large, barred pyroxene chondrule in Semarkona (#37) mostly had micro-crystallite-free mesostasis. Typically, such morphology within mesostasis yields high enough Al/Mg ratios (>50) that are favourable for $^{26}$Al–$^{26}$Mg isotope analysis. However, in this case, the different mesostasis regions were uniform with low Al/Mg, yielding an unresolved isochron. However, some of the data were resolved from the chondritic ratio and corresponded to the typical abundance of $^{26}$Al/$^{26}$Al of ~$1 \times 10^{-5}$ seen in the majority of the chondrules in Semarkona and unequilibrated ordinary chondrites.

A plagioclase-rich chondrule in Chainpur is also a rare object in unequilibrated chondrites that is potentially useful for $^{26}$Al–$^{26}$Mg isotopic systematics. However, the chondrule's broken periphery and crisscrossing fluid veins have most probably facilitated the diffusion and exchange of Al, Mg isotopes within the chondrule. The resulting fluid-assisted mobilization of elements is low Al/Mg regions within the chondrule that yield resolved excesses in $^{26}$Mg that is unsupported (discordant) concurrently with unresolved $^{26}$Mg isotopic ratios of the high $^{27}$Al/$^{24}$Mg regions within the chondrule. Nonetheless, few analyses within the chondrule were consistent with the typical $^{26}$Al abundances ($^{26}$Al/$^{27}$Al ~$1 \times 10^{-5}$) inferred for chondrules.

The $^{26}$Al–$^{26}$Mg isotopic records in the two chondrules from QUE 99177, though unresolved, were consistent with previous observations of most of the chondrules in CR chondrites[52–54], which showed lower $^{26}$Al/$^{27}$Al (<$3 \times 10^{-6}$) compared to UOCs[22,23,30,55,56] and carbonaceous organs chondrite[57–59].

## Summary and conclusions

The short-lived relative chronology using $^{26}$Al–$^{26}$Mg ($t_{1/2}$ = 0.72 Ma) isotope systematics in two CAIs and four chondrules from unequilibrated chondrites of low petrographic type (3.0–3.4) were carried out. The key features of the detailed petrographic studies of CAIs and some chondrules along with the isotopic studies are:

Leoville CAI 1, a typical Type B2 CAI was formed by partial melting of precursor dust, solid and gas at $T_{max}$ temperature of ~1420°C for a short period (a few tens of minutes – < hour), and cooling at a rate of ≤0.5°C/h. The *P–T* conditions fostered the formation of large melilite grains with decreasing gehlenitic composition towards the periphery, at times also showing reverse and or oscillatory zoning in the outer peripheral zones. At lower temperatures (~1250°C), pyroxene crystallization began, which increased the abundance of Al in the bulk melt, resulting in the reverse zoning in melilite. After a short time, plagioclase also began to crystallize alongside melilite and pyroxene at a tardy rate of cooling. The CAI, during a later episode, witnessed a high-temperature event that melted and evaporated the less refractory elements (Mg, Si) of the mineral phases (predominantly melilite) present in the peripheral regions leading to the formation of a WL-rim. $^{26}$Al abundance in melilite and anorthite in the inner regions of the CAI yield radiogenic excesses in $^{26}$Mg that suggest the formation of CAI at ~0.08 ± 0.07 Ma after canonical CAI formation. A relatively later time of formation (~0.1 Ma) of such large Type B from Efremovka, Vigarano and Allende has been previously explained as multi-epoch events of formations of CAIs.

Leoville CAI 3 has a simple gas-to-solid, multi-layered nodule formation from a cooling parcel of solar gas that was later aggregated by gentle collision and/or mild sintering. The CAI experienced metamorphism and morphological de(re)formation in the parent body that partially disturbed/reset the Al–Mg isotopic records of the CAI.


1. Davis, A. M. and McKeegan, K. D., Short-lived radionuclides and early solar system chronology. In *Meteorites, Comets, and Planets, Treatise on Geochemistry. Vol. 1: Meteorites and Cosmochemical Processes* (ed. Davis, A. M.), Elsevier, Oxford, 2014, 2nd edn, pp. 139–179.
2. Chaussidon, M. and Liu, M.-C., Timing of nebula processes that shaped the precursors of the terrestrial planets. In *The Early Earth: Accretion and Differentiation* (eds Badro, J. and Walters, M. J.), AGU Monograph, John Wiley, New Jersey, 2015, pp. 1–26.
3. Larsen, K. K. *et al.*, Episodic formation of refractory inclusions in the solar system and their presolar heritage. *Earth Planet. Sci. Lett.*, 2020, **535**, 22–24.
4. Krot, A. N., Keil, K., Scott, E. R. D., Goodrich, C. A. and Weisberg, M. K., Classification of meteorites and their genetic relationships. In *Meteorites, Comets, and Planets, Treatise on Geochemistry. Vol. 1: Meteorites and Cosmochemical Processes* (ed. Davis, A. M.), Elsevier, Oxford, 2014, 2nd edn, pp. 65–137.
5. Huss, G. R., Rubin, A. E. and Grossman, J. N., Thermal metamorphism in chondrites. In *Meteorites and the Early Solar System II* (eds Lauretta, D. S. and McSween Jr, H. Y.), University Arizona Press, Tuscon, 2006, pp. 567–586.
6. Bonal, L., Quirico, E., Bourot-Denise, M. and Montagnac, G., Determination of the petrologic type of CV3 chondrites by Raman spectroscopy of included organic matter. *Geochim. Cosmochim. Acta*, 2006, **70**, 1849–1863.
7. Kimura, M., Grossman, J. N. and Weisberg, M. K., Fe–Ni metal in primitive chondrites: indicators of classification and metamorphic conditions for ordinary and CO chondrites. *Meteorit. Planet. Sci.*, 2008, **43**, 1161–1177.
8. Mishra, R. K., Marhas, K. K. and Trieloff, M., $^{26}$Al–$^{26}$Mg isotope systematics in Leoville CAIs and Chainpur chondrule. In 49th Lunar and Planetary Science Conference, Lunar and Planetary Institute, Houston, 2018, p. 1633.
9. Luu, Tu-Han, Chaussidon, M., Mishra, R. K., Rollion-Bard, C., Villeneuve, J., Srinivasan, G. and Birck, J. L., High precision Mg isotope measurements of meteoritic samples by secondary ionization mass spectrometry. *J. Anal. Atom. Mass Spectrom.*, 2013, **28**, 67–76.
10. Catanzaro, E. J., Murphy, T. J., Garner, E. L. and Shields, W. R., Absolute isotopic abundance ratios and atomic weight of magnesium. *J. Res. Natl. Bur. Stand., Sect. A: Phys. Chem.*, 1966, **70**, 453–458.
11. Davis, A. M., Richter, F. M., Mendybaev, R. A., Janney, P. E., Wadhwa, M. and McKeegan, K. D., Isotopic mass fractionation laws for magnesium and their effects on $^{26}$Al–$^{26}$Mg systematics in solar system materials. *Geochim. Cosmochim. Acta*, 2015, **158**, 245–261.

12. Russell, S. S., Srinivasan, G., Huss, G. R., Wasserburg, G. J. and MacPherson, G. J., Evidence for widespread $^{26}$Al in the solar nebula and constraints for nebula timescales. *Science*, 1996, **273**, 757–762.
13. Huss, G. R., MacPherson, G. J., Wasserburg, G. J., Russell, S. S. and Srinivasan, G., Aluminum-26 in calcium–aluminum-rich inclusions and chondrules from unequilibrated ordinary chondrites. *Meteorit. Planet. Sci.*, 2001, **36**, 975–997.
14. Itoh, S., Russell, S. S. and Yurimoto, H., Oxygen and magnesium isotopic compositions of amoeboid olivine aggregates from the Semarkona LL3.0 chondrite. *Meteorit. Planet. Sci.*, 2007, **42**, 1241–1247.
15. Mishra, R. K., Simon, J. I., Ross, D. K. and Marhas, K. K., CAIs in Semarkona (LL3.0). In 47th Lunar and Planetary Science Conference, Lunar and Planetary Institute, Houston, 2016, p. 2750.
16. Mishra, R. K., Marhas, K. K. and Samir, Abundance of $^{60}$Fe inferred from nanoSIMS study of QUE 97008 (L3.05) chondrules. *Earth Planet. Sci. Lett.*, 2016, **436**, 71–81.
17. Russell, S. S., Itoh, S., Salge, T., Higashi, Y., Kawasaki, N. and Sakamoto, N. A., CAI in the highly unequilibrated ordinary chondrite Northwest Africa 8276: Implications for CAI formation and processing. In 47th Lunar and Planetary Science Conference, Lunar and Planetary Institute, Houston, 2016, p. 1989.
18. Haugbolle, T., Weber, P., Wielandt, D. P., Benitez-Llambay, P., Bizzarro, M., Gressel, O. and Pessah, M. E., Probing the protosolar disk using dust filtering at gaps in the early solar system. *Astrophys. J.*, 2019, **158**, 17.
19. MacPherson, G. J., Krot, A. N. and Nagashima, K., Al–Mg isotopic study of spinel-rich fine-grained CAIs. *Meteorit. Planet. Sci.*, 2020, **55**, 2519–2538.
20. Mishra, R. K., Petrography and mineralogy of a large calcium, aluminum-rich inclusion in Chainpur (LL3.4) ordinary chondrite. In 52nd Lunar and Planetary Science Conference, Lunar and Planetary Institute, Houston, 2021, p. 1837.
21. Kita, N. T., Nagahara, H., Togashi, S. and Morishita, Y., A short duration of chondrule formation in the solar nebula: evidence from $^{26}$Al in Semarkona ferromagnesian chondrules. *Geochim. Cosmochim. Acta*, 2000, **64**, 3913–3922.
22. Rudraswami, N. G., Goswami, J. N., Chattopadhyay, B., Sengupta, S. K. and Thapliyal, A. P., $^{26}$Al records in chondrules from unequilibrated ordinary chondrites: II. Duration of chondrule formation and parent body thermal metamorphism. *Earth Planet. Sci. Lett.*, 2008, **274**, 93–102.
23. Villeneuve, J., Chaussidon, M. and Libourel, G., Homogeneous distribution of $^{26}$Al in the solar system from the mg isotopic composition of chondrules. *Science*, 2009, **325**, 985–988.
24. Mishra, R. K., Records of now-extinct nuclides in early solar system objects: an ion microprobe study. Doctoral Thesis, Gujarat University, India, 2009.
25. Mishra, R. K. and Chaussidon, M., $^{60}$Fe–$^{60}$Ni isotope systematics in silicates in chondrules from unequilibrated chondrites: yet again and status quo. *Meteorit. Planet. Sci.*, 2012, **47**, 5194.
26. Mishra, R. K. and Chaussidon, M., Fossil records of high level of $^{60}$Fe in chondrules from unequilibrated chondrites. Timing and extent of Mg and Al isotopic homogenization in the early solar system. *Earth Planet. Sci. Lett.*, 2014, **398**, 90–100.
27. Mishra, R. K., Goswami, J. N., Tachibana, S., Huss, G. R. and Rudraswami, N. G., $^{60}$Fe and $^{26}$Al in chondrules from unequilibrated chondrites: implications for early Solar system processes. *Astrophys. J. Lett.*, 2010, **714**, L217–L221.
28. MacPherson, G. J. and Huss, G. R., Petrogenesis of Al-rich chondrules: Evidence from bulk compositions and phase equilibria. *Geochim. Cosmochim. Acta*, 2005, **69**, 3099–3127.
29. Abreu, N. and Brearley, A., Early solar system processes recorded in the matrices of two highly pristine CR3 carbonaceous chondrites, MET 00426 and QUE 99177. *Geochim. Cosmochim. Acta*, 2010, **74**, 1146–1171.
30. Pape, J., Mezger, K., Bouvier, A.-S. and Baumgartner, L. P., Time and duration of chondrule formation: constraints from $^{26}$Al–$^{26}$Mg ages of individual chondrules. *Geochim. Cosmochim. Acta*, 2018, **244**, 416–436.
31. Stolper, E. and Paque, J. M., Crystallization sequence of Ca–Al-rich inclusions from Allende: the effects of cooling rate and maximum. *Geochim. Cosmochim. Acta*, 1986, **50**, 1785–1806.
32. Paque, J. M., Lofgren, G. E. and Loan, L., Crystallization of calcium–aluminum-rich inclusions: experimental studies on the effects of led heating events. *Meteorit. Planet. Sci.*, 2000, **35**, 363–371.
33. Ebel, D. S., Condensation of rocky material in astrophysical environments. In *Meteorites and the Early Solar System II* (eds Lauretta, D. S. and McSween Jr, H. Y.), University Arizona Press, Tuscon, 2006, pp. 253–277.
34. Petaev, M. I. and Jacobsen, S. B., Petrologic study of SJ101, a new forsterite-bearing CAI from the Allende CV3 chondrite. *Geochim. Cosmochim. Acta*, 2009, **73**, 5100–5114.
35. MacPherson, G. J., Calcium-aluminum-rich inclusions in chondritic meteorites. In *Meteorites, Comets, and Planets, Treatise on Geochemistry. Vol. 1: Meteorites and Cosmochemical Processes* (ed. Davis, A. M.), Elsevier, Oxford, 2014, 2nd edn, pp. 201–246.
36. Amelin, Y., Kaltenbach, A., Lizuka, T., Stirling, C. H., Ireland, T. R., Petaev, M. and Jacobsen S. B., U–Pb chronology of the Solar system's oldest solids with variable $^{238}$U/$^{235}$U. *Earth Planet. Sci. Lett.*, 2012, **300**, 343–350.
37. Bouvier, A. and Wadhwa, M., The age of the solar system redefined by the oldest Pb–Pb age of a meteoritic inclusion. *Nat. Geosci.*, 2010, **3**(9), 637–641.
38. Connelly, J. N., Bizzarro, M., Krot, A. N., Nordlund, Å., Wielandt, D. and Ivanova, M. A., The absolute chronology and thermal processing of solids in the solar protoplanetary disk. *Science*, 2012, **338**, 651–655.
39. Kita, N. T. *et al.*, $^{26}$Al–$^{26}$Mg isotope systematics of the first solids in the early solar system. *Meteorit. Planet. Sci.*, 2013, **483**, 1383–1400.
40. Mishra, R. K. and Chaussidon, M., Timing and extent of Mg and Al isotopic homogenization in the early solar system. *Earth Planet. Sci. Lett.*, 2014, **390**, 318–326.
41. Kawasaki, N., Park, C., Sakamoto, N., Park, S., Kim, H., Kuroda, M. and Yurimoto, H., Variations in initial $^{26}$Al/$^{27}$Al ratios among fluffy Type A Ca–Al-rich inclusions from reduced CV chondrites. *Earth Planet. Sci. Lett.*, 2019, **511**, 25–35.
42. Kawasaki, N., Itoh, S., Sakamoto, N. and Yurimoto, H., Chronological study of oxygen isotope composition for the solar protoplanetary disk recorded in a fluffy Type A CAI from Vigarano. *Geochim. Cosmochim. Acta*, 2017, **201**, 83–102.
43. Mishra, R. K. and Marhas, K. K., Meteoritic evidences of a late superflare as source of $^{7}$Be in the early solar system. *Nat. Astron.*, 2019, **3**, 498–505.
44. Goswami, J. N., Srinivasan, G. and Ulyanov, A. A., Ion microprobe studies of Efremovka CAIs. 1. Magnesium isotope composition. *Geochim. Cosmochim. Acta*, 1994, **58**, 431–447.
45. Marhas, K. K. and Mishra, R. K., The vanguard of irradiation: the fourth element. In 49th Lunar and Planetary Science Conference, Lunar and Planetary Institute, Houston, 2018, p. 1646.
46. Kita, N. T., Ushikubo, T., Knight, K. B., Mendybeav, R. A., Davis, A. M., Ritcher, F. M. and Fournelle, J. H., Internal $^{26}$Al–$^{26}$Mg isotope systematics of a Type B CAI: remelting of refractory precursor solids. *Geochim. Cosmochim. Acta*, 2012, **86**, 37–51.
47. Larsen, K. K. *et al.*, Evidence for magnesium isotope heterogeneity in the solar protoplanetary disk. *Astrophys. J. Lett.*, 2011, **735**, L37–L44.
48. Olsen, M. B., Wielandt, D., Schiller, M., Van Kooten, E. M. M. E. and Bizzarro, M., Magnesium and $^{54}$Cr isotope compositions of carbonaceous chondrite chondrules – insights into early disk processes. *Geochim. Cosmochim. Acta*, 2016, **191**, 118–138.
49. Bollard, J. *et al.*, Combined U-corrected Pb–Pb dating and $^{26}$Al–$^{26}$Mg systematics of individual chondrules – evidence for a reduced

initial abundance of $^{26}$Al amongst inner solar system chondrules. *Geochim. Cosmochim. Acta*, 2019, **260**, 62–83.
50. Kööp, L. *et al.*, A link between oxygen, calcium, and titanium isotopes in $^{26}$Al-poor hibonite-rich CAIs from Murchison and implications for the heterogeneity of dust reservoirs in the solar nebula. *Geochim. Cosmochim. Acta*, 2016, **189**, 70–95.
51. Kööp, L. *et al.*, New constraints on the relationship between $^{26}$Al and oxygen, calcium, and titanium isotopic variation in the early Solar system from a multiple isotopic study of spinel-hibonite inclusion. *Geochim. Cosmochim. Acta*, 2016, **184**, 151–172.
52. Nagashima, K., Krot, A. N. and Huss, G. R., $^{26}$Al in chondrules from CR2 chondrites. *Geochem. J.*, 2014, **48**, 561–570.
53. Schrader, D. L. *et al.*, Distribution of $^{26}$Al in the CR chondrite chondrule-forming region of the protoplanetary disk. *Geochim. Cosmochim. Acta*, 2017, **201**, 275–302.
54. Tenner, T. J., Nakashima, D., Ushikubo, T., Tomioka, N., Kimura, M., Weisberg, M. K. and Kita, N. T., Extended chondrule formation intervals in distinct physicochemical environments: evidence from Al–Mg isotope systematics of CR chondrite chondrules with unaltered plagioclase. *Geochim. Cosmochim. Acta*, 2019, **260**, 133–160.
55. Rudraswami, N. G. and Goswami, J. N., $^{26}$Al in chondrules from unequilibrated L chondrites: Onset and duration of chondrule formation in the early solar system. *Earth Planet. Sci. Lett.*, 2007, **257**, 231–244.
56. Siron, G., Fukuda, K., Kimura, M. and Kita, N. T., New constraints from $^{26}$Al–$^{26}$Mg chronology of anorthite bearing chondrules in unequilibrated ordinary chondrites. *Geochim. Cosmochim. Acta*, 2021, **293**, 103–126.
57. Russell, S. S., Huss, G. R., Fahey, A. J., Greenwood, R. C., Hutchison, R. and Wasserburg, G. J., An isotopic and petrologic study of calcium–aluminum-rich inclusions from $CO_3$ meteorites. *Geochim. Cosmochim. Acta*, 1998, **62**, 689–714.
58. Kurahashi, E., Kita, N. T., Nagahara, H. and Morishita, Y., $^{26}$Al–$^{26}$Mg isotope systematics of chondrules in primitive CO chondrite. *Geochim. Cosmochim. Acta*, 2008, **72**, 3865–3882.
59. Hutcheon, I. D., Marhas, K. K., Krot, A. N., Goswami, J. N. and Jones, R. H., $^{26}$Al in plagioclase-rich chondrules in carbonaceous chondrites: evidence for an extended duration of chondrule formation. *Geochim. Cosmochim. Acta*, 2009, **73**, 5080–5099.

ACKNOWLEDGEMENTS. We thank NASA ANSMET program for lending a thin section of QUE 99177. R.K.M. thanks Dr D. K. Ross (Johnson Space Center, Houston) for providing generous assistance during mapping and quantitative analyses of some of the objects. We also thank Prof. R. Srinivasan for the comments, suggestions on the manuscript that helped improve it. The financial support during the work by NASA Post-doctoral program Fellowship at NASA Johnson Space Center, Houston is acknowledged. The experimental work and manuscript was prepared during the Humboldt Fellowship at Ruprecht-Karls-Universität, Heidelberg. Financial support from the Alexander Von Humboldt Foundation during the term is also acknowledged. K.K.M. acknowledges research support under SERB-POWER fellowship (grant no. SPF/2021/000116) from Scientific and Research Board (SERB), India and Indo-French research grant under CEFIPRA (6407-A) program.

Received 5 September 2022; revised accepted 3 May 2023

doi: 10.18520/cs/v125/i2/191-203